



This is a repository copy of *Fluorinated solid additives enable high efficiency non-fullerene organic solar cells*.

White Rose Research Online URL for this paper:
<http://eprints.whiterose.ac.uk/160401/>

Version: Accepted Version

Article:

Cai, J., Wang, H., Zhang, X. et al. (15 more authors) (2020) Fluorinated solid additives enable high efficiency non-fullerene organic solar cells. *Journal of Materials Chemistry A*, 8 (8). pp. 4230-4238. ISSN 2050-7488

<https://doi.org/10.1039/c9ta13974e>

© The Royal Society of Chemistry 2020. This is an author-produced version of a paper subsequently published in *Journal of Materials Chemistry A*. Uploaded in accordance with the publisher's self-archiving policy.

Reuse

Items deposited in White Rose Research Online are protected by copyright, with all rights reserved unless indicated otherwise. They may be downloaded and/or printed for private study, or other acts as permitted by national copyright laws. The publisher or other rights holders may allow further reproduction and re-use of the full text version. This is indicated by the licence information on the White Rose Research Online record for the item.

Takedown

If you consider content in White Rose Research Online to be in breach of UK law, please notify us by emailing eprints@whiterose.ac.uk including the URL of the record and the reason for the withdrawal request.



eprints@whiterose.ac.uk
<https://eprints.whiterose.ac.uk/>

Fluorinated solid additives enable high efficiency non-fullerene organic solar cells

Jinglong Cai^{ab}, Hui Wang^{ab}, Xue Zhang^{ab}, Wei Li^{ab}, Donghui Li^{ab}, Yuchao Mao^{ab}, Baocai Du^{ab}, Mengxue Chen^{ab}, Yuan Zhuang^{ab}, Dan Liu^{ab}, Hua-Li Qin^{bc}, Yan Zhao^d, Joel A. Smith^e, Rachel C. Kilbride^e, Andrew J. Parnell^e, Richard A.L. Jones^e, David G. Lidzey^e, Tao Wang^{ab*}

^aSchool of Materials Science and Engineering, Wuhan University of Technology, Wuhan 430070, China. E-mail: twang@whut.edu.cn

^bState Key Laboratory of Silicate Materials for Architectures, Wuhan University of Technology, Wuhan 430070, China

^cSchool of Chemistry, Chemical Engineering and Life Sciences, Wuhan University of Technology, Wuhan 430070, China

^dInternational School of Materials Science and Engineering, Wuhan University of Technology, Wuhan 430070, China

^eDepartment of Physics and Astronomy, University of Sheffield, Sheffield, S3 7RH, UK

Abstract

The use of processing additives to optimize active layer morphology in organic solar cells (OSCs) is a simple and impactful way to improve photovoltaic performance. However, the retention of high boiling point liquid additives affects the stability and lifetime of OSCs, necessitating the development of volatilizable additives that can improve efficiency at no cost to long-term device stability. In this study, three novel volatilizable solid additives, INB-1F, INB-3F, INB-5F, with different degrees of fluorination are rationally designed, synthesized, and added into photovoltaic solutions to fabricate OSCs. These additives evaporate upon thermal annealing and exhibit higher volatility as the number of fluorine atoms increases. Our device studies show that these additives can enhance the efficiency of PBDB-T-2F:BTP-4F binary cells from 15.2% to 16.5%, and those of PBDB-T-2F:IT-4F from 12.1% to 13.4%. Molecular dynamic simulations reveal attractive interactions between these additives and the non-fullerene acceptor BTP-4F, leading to enhanced intermolecular π - π stacking among BTP-4Fs, which is a favorable morphology change that we attribute as the origin of the enhanced performance and long-term stability. Our work presents a novel strategy to design new solid additives to replace liquid additives.

Keywords: fluorinated solid additives, morphology, power conversion efficiency

1. Introduction

Bulk heterojunction organic solar cells (OSCs) are considered promising technology for the realization of renewable solar energy conversion for their attractive advantages, e.g. lightweight, low-cost and the feasibility of manufacturing large-area devices on mechanically flexible substrate using solution casting methods.¹⁻⁵ Besides, semitransparent or fully transparent OSCs can also be integrated with building to extend their applications.⁶⁻⁷ New donor and acceptor materials, especially non-fullerene small molecule acceptors (NFAs) like BTP-4F (also known as Y6), drive the steady progress of OSCs.⁸⁻¹⁰ The employment of these new semiconductors¹¹⁻¹³, morphology control¹⁴⁻¹⁵, interfacial engineering¹⁶⁻¹⁷ and device architecture design¹⁸⁻¹⁹ have boosted the maximum achievable power conversion efficiencies (PCEs) of OSCs to over 16% in single-junction OSCs and over 17% in tandem OSCs.^{8,20-24} However, the majority of OSCs achieving over 16% PCEs necessarily employ a ternary strategy (i.e. with more than one donor/acceptor pairs in the photoactive layer) to achieve complementary light absorption and superior optoelectronic properties.^{23-24,25-28}

Morphology control steps¹⁴, such as thermal annealing²⁹⁻³⁰, vapor annealing³¹⁻³², hot-substrate casting^{15,33} and solvent additive modulation³⁴⁻³⁷ have been shown to be effective and crucial to realize the maximum achievable PCEs. Among these approaches, solvent additives can effectively regulate the molecular packing and orientation of electron donors and acceptors from the solution state through to the vitrified solid films, as well as tuning the phase-separated domain size, purity and connectivity, which ultimately determines the device PCE.³⁸ The selection of solvent additives for non-fullerene OSCs has largely relied on lessons drawn from fullerene-based OSCs, which traditionally use high boiling point additives like 1,8-diiodooctane (DIO)³⁹, diphenyl ether (DPE)⁴⁰ and 1-chloro-naphthlene (1CN)⁴¹. These additives have been found to reside longer than the primary solvent in the dried films and undergo preferential interaction with PCBM to manipulate its packing and aggregation. Although these additives appear to be effective, they tend to reside in the photoactive layer of OSCs unless they are deliberately removed via further treatments. The presence of such additives can lead to instability of the nano-morphology as well as reduced device efficiency.⁴²⁻⁴³ When using additives with non-fullerene OSCs, it has been found that they may not help to improve device efficiency at all.⁴⁴ Recently, novel aromatic solid additives have emerged and have been investigated. For example, Hou et al. reported the design and application of volatile solid additives to improve the efficiency of non-fullerene OSCs.⁴⁵⁻⁴⁶ However, with the exception

of these reports, new volatile additives are still rare in the literature, and a variety of solid additives are of high interest to effectively regulate the morphology and efficiency of non-fullerene OSCs.

Here, we explore three volatilizable organic solid additives with different degrees of fluorination, namely INB-1F (2-(4-fluorobenzylidene)-1H-indene-1,3(2H)-dione), INB-3F (2-(2,4,6-trifluorobenzylidene)-1H-indene-1,3(2H)-dione), and INB-5F (2-((perfluorophenyl)methylene)-1H-indene-1,3(2H)-dione). These materials were designed, synthesized and utilized in non-fullerene OSCs with two typical non-fullerene OSCs, PBDB-T-2F:IT-4F and PBDB-T-2F:BTP-4F to investigate their role in controlling morphology and PCE. These additives evaporate upon thermal annealing at a temperature of 110 °C for 10 minutes, and show increasing volatility as the number of fluorine atoms increases. Molecular dynamic simulations reveal attractive interactions between these additives and the non-fullerene acceptor BTP-4F, leading to enhanced π - π stacking among BTP-4Fs that is supported by grazing incidence wide-angle X-ray scattering experiments. In comparison to binary OSCs processed without additives, the maximum achievable PCE was enhanced from 12.1% to 13.4%, and from 15.2% to 16.5% for PBDB-T-2F:IT-4F and PBDB-T-2F:BTP-4F OSCs respectively. Our work demonstrates that such volatilizable yet solid additives can be used to manipulate the molecular packing and morphology and thereby enhance device efficiency and stability, and present a new impetus to design solid additives to replace high boiling point liquid additives.

2. Results and discussion

The chemical structures of PBDB-T-2F, BTP-4F, IT-4F, and additives INB-1F, INB-3F, INB-5F designed in this work, are shown in Fig. 1. In order to obtain good miscibility of additives with NFAs, we started with the typical terminal group 1H-indene-1, 3(2H)-dione of NFAs, and attached to it benzaldehyde moieties with different number of fluorine atoms to obtain the target solid additives through the classic Knoevenagel condensation reaction (Scheme S1, Supporting Information). Compared to the solid additives reported by Hou's group⁴⁵⁻⁴⁶, the fluorine atoms on the benzaldehyde unit of additives in this work increase the electron delocalization on the benzene ring, potentially can lead to different interactions with non-fullerene acceptors. These additives all demonstrate good solubility in common organic solvents, such as chloroform, dichloromethane, chlorobenzene, o-dichlorobenzene. As illustrated in Fig. 2(b), INB-1F, INB-3F, INB-5F dissolved in chloroform have an absorption peak at 347, 330 and 327 nm, respectively. As the number of

fluorine atoms on the benzaldehyde unit increases, the absorption spectrum of the additive gradually blue-shifts. The absorption peaks all red shift and broaden in thin films. These additives are solid after synthesis, but are volatile and can be sublimed by heating thin films to modest temperatures. As shown in Fig. 2(a), the spin-coated additive films virtually disappear after thermal annealing at 110 °C for 10 min. To further confirm their volatility, the changes of thickness of pure INB-1F, INB-3F, INB-5F films (determined by spectroscopic ellipsometry) subject to increasing temperature or time are shown in Fig. 2(c-d). By either increasing the annealing temperature with a fixed annealing time, or prolonging the annealing time under a fixed temperature, INB-1F, 3F, 5F molecules evaporate gradually. For example, by annealing at 110 °C for 10 mins, the thickness of all pure additive films reduces to less than 20% of its initial thickness and the intensity of the UV-Vis spectrum reduces to nearly zero (see Fig. S1), demonstrating significant volatility. Additionally, as the number of fluorine atoms increases, the additive becomes more volatile.

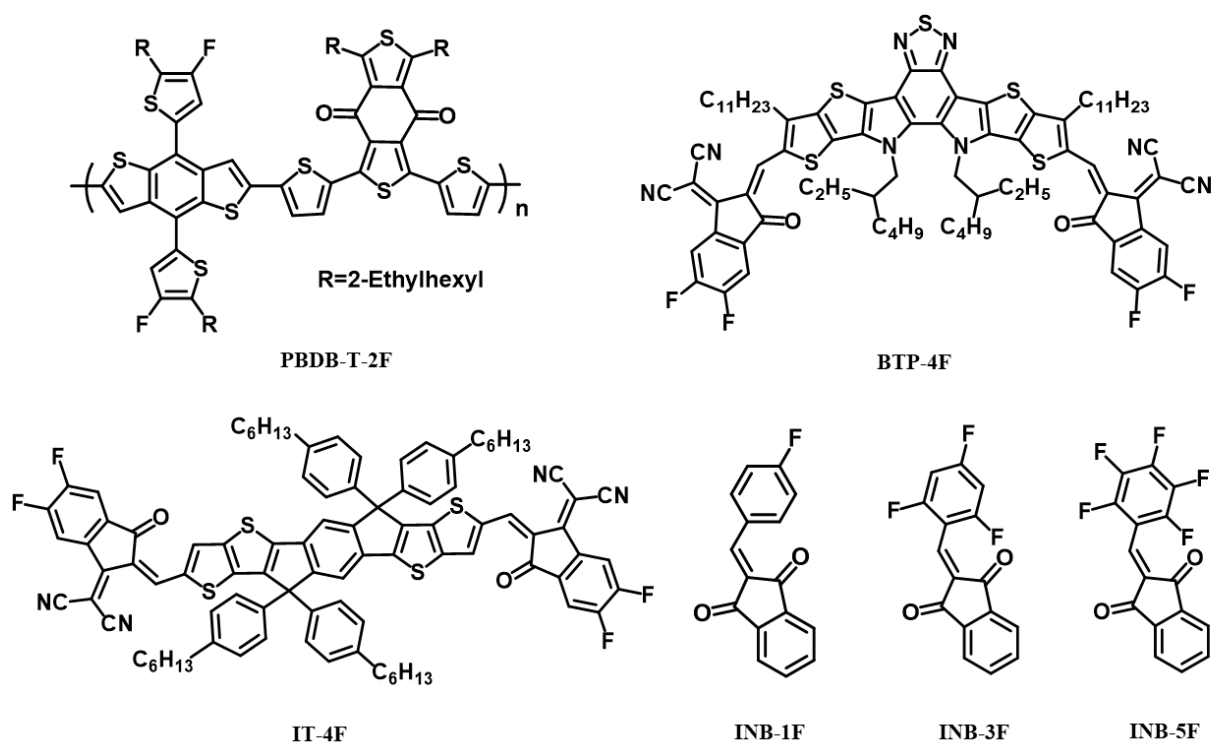


Fig. 1 Chemical structures of PBDB-T-2F, BTP-4F, IT-4F and three OPV processing additives INB-1F, INB-3F and INB-5F.

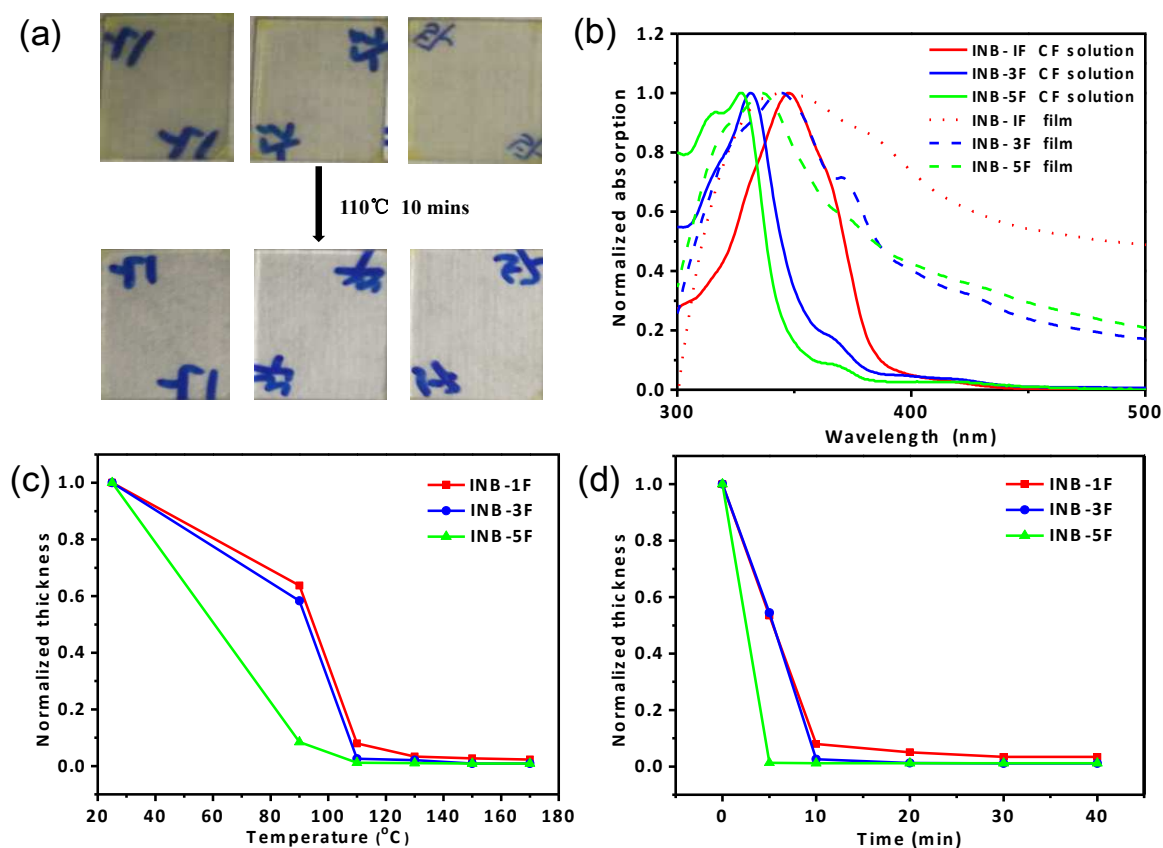


Fig. 2 (a) Photographs of pure additive films before and after thermal annealing. (b) Normalized absorption of three additives in chloroform solution and pure films. Normalized film thicknesses after baking (c) for 10 mins under different temperature, and (d) under 110 °C as a function of time.

The content of the additives and the annealing temperature were firstly optimized using INB-1F as an example with PBDB-T-2F:BTP-4F OSCs, having a device structure of ITO/ZnO/PBDB-T-2F:BTP-4F/MoO₃/Ag. INB-1F was added at various concentrations with respect to the NFA at mole ratios of 1:0, 1:0.2, 1:0.5 and 1:1. The device J-V curves are plotted in Figure S2 and the device metric are summarized in Table S1, from which we identify that the optimal additive content is BTP-4F:INB-1F=1:0.5, and the optimal annealing temperature is 110 °C for 10 min. Upon annealing at this condition, the thickness of the active layer is typically reduced from 140 nm for the as-cast films containing additives, to 120 nm (which is an optimized thickness of the photoactive layer and is consistent with previous work¹⁰). This process results in increased film optical absorption as a result of densification and morphological changes which we will discuss below. The UV-Vis spectra of BTP-4F neat films processed with and without additives, in an as-cast state and after thermal annealing, are plotted in Fig. 3(a). Compared with the pure BTP-4F film, the absorption spectra of films processed with additives red-shifts around 13 nm with increased intensity, which could be ascribed to the enhanced intermolecular π - π interaction among

BTP-4F molecules. The characteristic absorption peaks of INB-1F, 3F, 5F in the range of 300~400 nm disappear after thermal annealing, but the intensity of the primary absorption peak of BTP-4F further increases and red-shifts, with the INB-5F additive being most effective. The absorbance of PBDB-T-2F:BTP-4F binary films processed with INB-1F, INB-3F, INB-5F at a fixed molar ratio (half that of BTP-4F) and further treated with/without thermal annealing are shown in Fig. 3(b). A similar phenomenon can be observed in the PBDB-T-2F:BTP-4F-based blend film. The pure PBDB-T-2F:BTP-4F film without the presence of any additives and annealing exhibits three main and broad absorption peaks at *ca.* 313, 622 and 802 nm. After processed with INB-1F, INB-3F and INB-5F, the absorption increases in all cases and is strongest for the INB-5F additive. When these films were further processed by annealing, the peak in 300-400 nm vanishes due to the evaporation of these additives and the characteristic peak of BTP-4F is obviously red shifted with enhanced absorption coefficient, which is confirmed again that additives has good volatility and the obvious role on enhancing inter-molecular π - π stacking of electron acceptors. We note here that the location of the peak at 622 nm, which is mainly attribute to the donor PBDB-T, has not been shifted, suggesting limited effect of these additives on regulating the π - π stacking of PBDB-T.

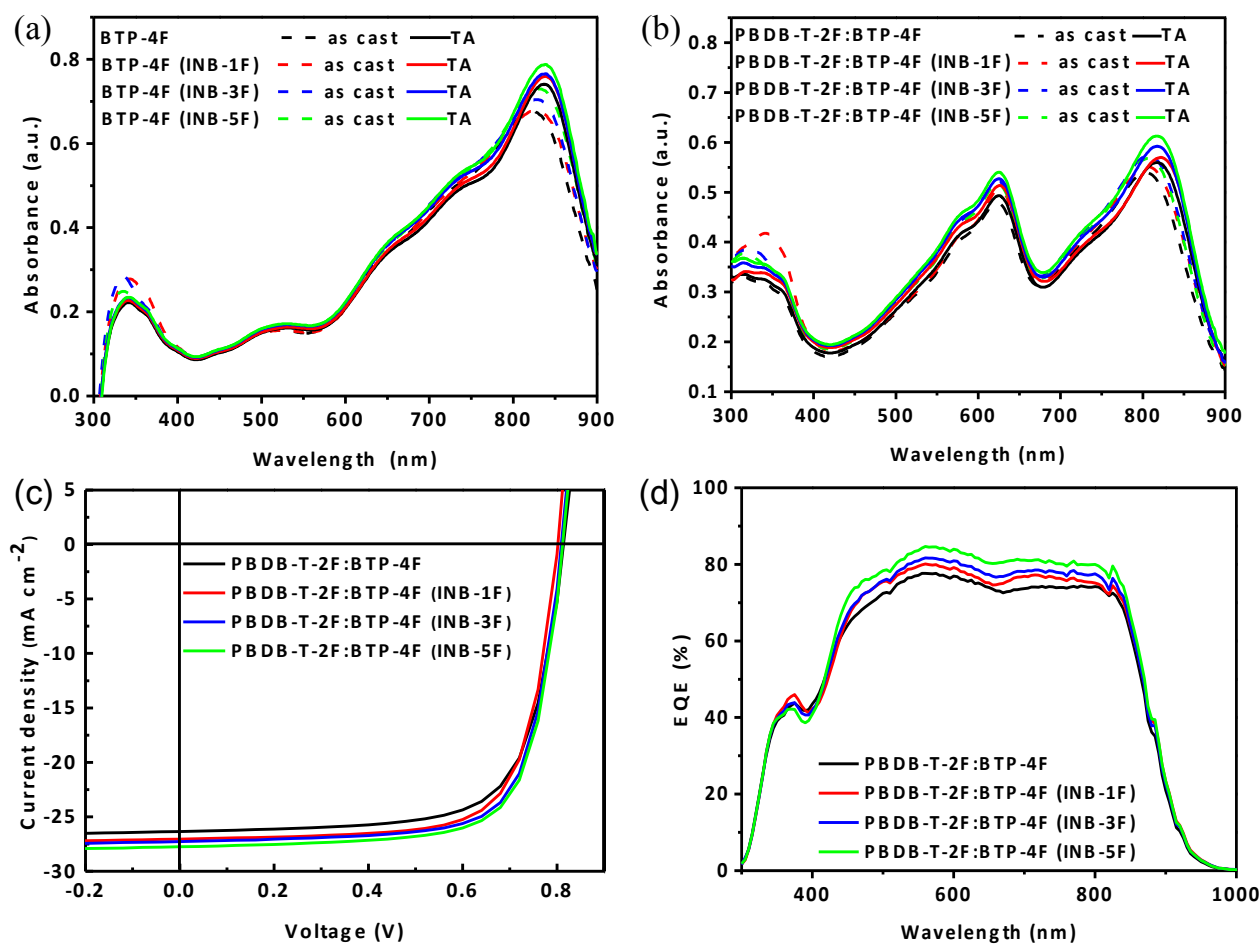


Fig. 3 (a) Absorbance of neat BTP-4F films processed with/without additives, and further treated with/without thermal annealing. (b) Absorbance of PBDB-T-2F:BTP-4F blend films processed with/without additives, and further treated with/without thermal annealing. (c) J-V characteristics and (d) EQE spectra of the corresponding PBDB-T-2F:BTP-4F devices.

Table 1 Device metrics for PBDB-T-2F:BTP-4F OSCs processed with/without solid additives. The standard deviations were obtained from 20 devices.

Active layer composition	V_{oc} [V]	J_{sc} [mA cm ⁻²]	Calculated J_{sc} [mA cm ⁻²]	FF [%]	PCE [%]
PBDB-T-2F:BTP-4F	0.82±0.00	26.2±0.4	25.7	70.1±1.3	15.1±0.1(15.2)
PBDB-T-2F:BTP-4F (INB-1F)	0.81±0.00	27.0±0.2	26.5	72.0±0.2	15.7±0.2(15.8)
PBDB-T-2F:BTP-4F (INB-3F)	0.81±0.00	27.1±0.2	26.7	72.2±0.5	15.8±0.1(15.9)
PBDB-T-2F:BTP-4F (INB-5F)	0.81±0.00	27.7±0.1	27.1	74.3±0.3	16.4±0.1(16.5)

The current density-voltage (J-V) characteristics of PBDB-T-2F:BDP-4F OSCs are plotted in Fig. 3(c) and the corresponding device metrics are summarized in Table 1. For the reference device without any additives, a maximum PCE of 15.2% with an average V_{oc} of 0.82±0.00 V, J_{sc} of 26.2±0.4 mA cm⁻² and FF of 70.1±1.3% were obtained. When the films were treated with these additives, the J_{sc} and FF both improved (although the device V_{oc} decreased slightly from 0.82 to 0.81 V), leading to an increase in the maximum PCEs of 15.8%, 15.9% and 16.5% for the additives INB-1F, INB-3F and INB-5F respectively. The external quantum efficiency (EQE) of such OSCs is shown in Fig. 3(d); here we observe a broad response over the wavelength range 300 to 950 nm. When the device was processed using INB-1F, INB-3F and INB-5F, the spectral response increased, particularly over the spectral region from 400 to 850 nm; a result consistent with the enhanced device J_{sc} . Calculated J_{sc} values from integrating the EQE spectra are 26.5, 26.7 and 27.1 mA cm⁻² for devices processed with INB-1F, INB-3F and INB-5F respectively. These values are only *ca.* 5% less than the J_{sc} values obtained from the J-V testing, and confirm the validity of our J-V measurements.

To determine whether the effect of these solid additives generalizes to other non-fullerene

OSC systems, PBDB-T-2F:IT-4F devices were also investigated. Fig. S3 shows the absorbance, J-V characteristics and EQE spectra of a reference PBDB-T-2F:IT-4F device and those processed with INB-1F, INB-3F and INB-5F. Table S2 summarizes specific device metrics. INB-1F, INB-3F and INB-5F additives are also found to increase the maximum PCE of PBDB-T-2F:IT-4F devices to 13.0%, 13.1% and 13.4% for each of the three additives, from a reference of 12.2%. This demonstrates that the benefits of these additives are not limited to one specific material system but can actually enhance device performance in many non-fullerene OSCs.

To further understand how these solid additives can enhance device performance, we return to the champion system PBDB-T-2F:BTP-4F. Firstly, a space charge-limited current (SCLC) method⁴⁷⁻⁴⁸ was used to characterize the charge mobility of PBDB-T-2F:BTP-4F from dark J-V curves of hole-only and electron-only devices (see Fig. S4, and Table S3). The electron and hole mobilities of the reference PBDB-T-2F:BTP-4F device are 5.9×10^{-4} and $1.6 \times 10^{-4} \text{ cm}^2 \text{ V}^{-1} \text{ s}^{-1}$ respectively, leading to a μ_e/μ_h ratio of 3.7. When the PBDB-T-2F:BTP-4F layer was processed with solid additives, both μ_e and μ_h increased but the μ_e/μ_h ratio became more balanced. Finding consistent with our observed enhancements in device efficiency, INB-5F increasing μ_e and μ_h to a maximum value of 7.9×10^{-4} and $3.2 \times 10^{-4} \text{ cm}^2 \text{ V}^{-1} \text{ s}^{-1}$ respectively. This corresponds to a lowest μ_e/μ_h ratio of 2.5. To gain insights into the charge recombination mechanisms in the active layers, V_{OC} and J_{SC} of devices illuminated under different light intensity (P_{light}) were measured. As we can see from Fig. S5, the slopes of V_{OC} versus $\ln(P_{light})$ plots are 1.55, 1.19, 1.12 and 1.03 for the reference cell and those processed with INB-1F, INB-3F and INB-5F respectively, which confirms that devices treated with additives have reduced trap-assisted recombination compared with the reference device, and bimolecular recombination has become the main charge loss. Besides, the slope of $\log(J_{SC})$ versus $\log(P_{light})$ in the device processed with INB-5F is more close to 1 than others, associating with the weakest bimolecular recombination.⁴⁹⁻⁵⁰

The surface morphology of the PBDB-T-2F:BTP-4F films probed by atomic force microscopy (AFM) is shown in Fig. S6. We find the surfaces exhibit very similar morphology, with an absence of excessive clusters or holes on the film surface due to the evaporation of these solid additives. The average root-mean-square (RMS) roughness increased slightly from *ca.* 1 nm to 2 nm after processing with these three solid additives, demonstrating negligible impact towards the interface with the top electrode. Grazing-incidence wide-angle X-ray scattering (GIWAXS) measurements were used to characterise changes in molecular packing in the PBDB-T-2F:BTP-4F thin films. The

1D profiles along the out-of-plane (OOP) direction were extracted from the 2D GIWAXS patterns (see Fig. 4(a-d)) and are shown in Fig. 4(i). Literature reports⁹⁻¹⁰ indicate that pure PBDB-T-2F exhibits a (010) π - π stacking peak at $q_z=1.66 \text{ \AA}^{-1}$ in the OOP direction, and a (100) scattering peak at $q_{xy}=0.30 \text{ \AA}^{-1}$ in the in-plane (IP) direction that is associated with lamellar stacking. BTP-4F exhibits π - π stacking peak at $q_z=1.76 \text{ \AA}^{-1}$ and lamellar stacking around $q_{xy}=0.29$ and 0.42 \AA^{-1} . The scattering rings at $q_{xy}=0.30 \text{ \AA}^{-1}$ in Fig. 4(a-d) can be attributed to (100) of PBDB-T-2F or BTP-4F, whilst the crescent at $q_z=1.76 \text{ \AA}^{-1}$ can be assigned to the π - π stacking of BTP-4F. When the blend film was processed using three different additives, scattering from the π - π stacking at $q_z=1.76 \text{ \AA}^{-1}$ became more intense, especially in films processed using INB-3F and INB-5F (see Fig. 4(c-d) and in comparison with Fig. 4(i)), illustrating significantly enhanced face-on π - π stacking of the BTP-4F electron acceptor. This favorable “face-on” oriented molecular packing leads to improved electron mobility. It is notable that the (100) ring is also enhanced (see Fig. 4(c&d)), showing the same trend with the π - π stacking changes.

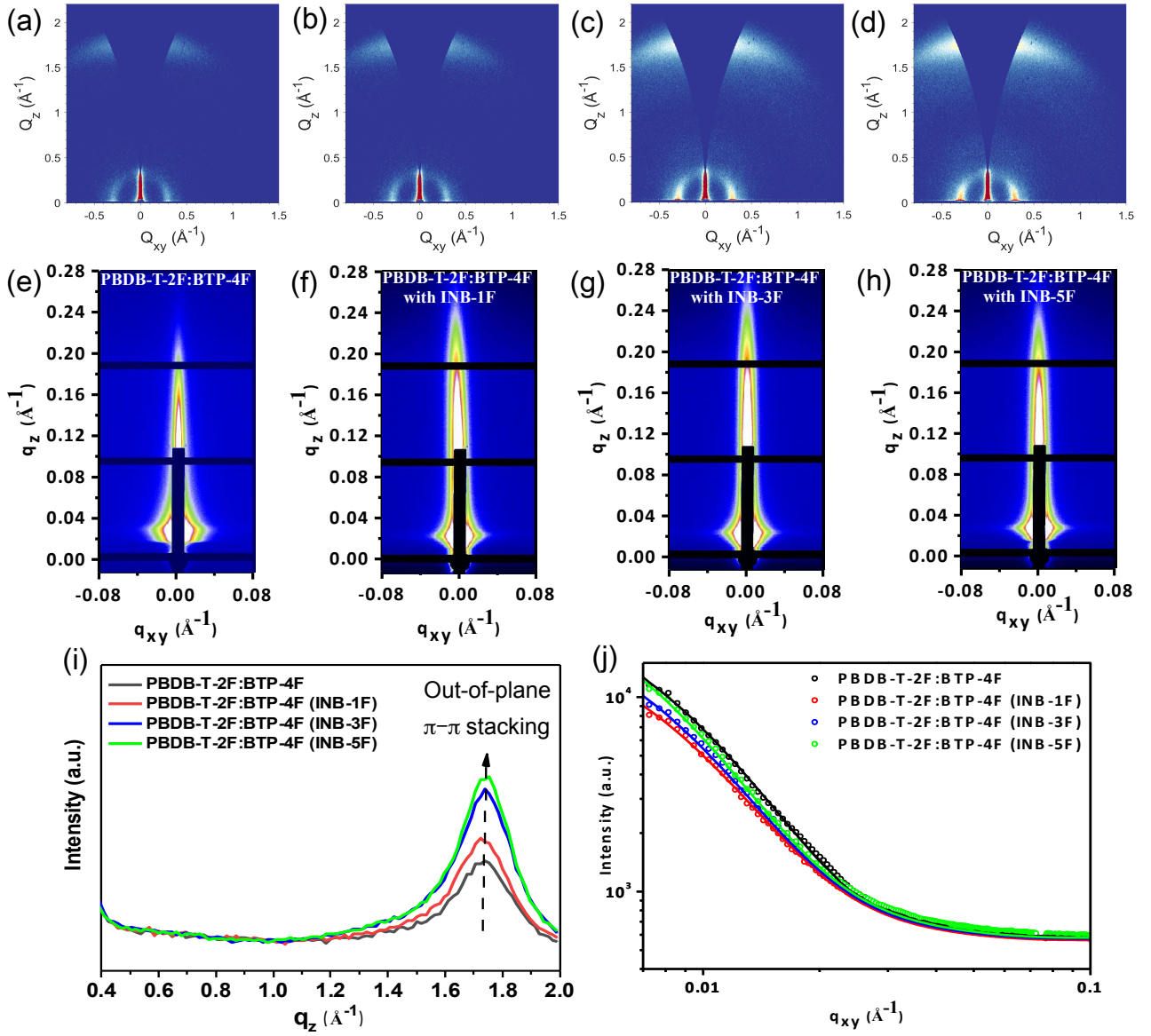


Fig. 4 2D GIWAXS patterns of (a) neat PBDB-T-2F:BTP-4F film, and those processed with (b) INB-1F, (c) INB-3F, (d) INB-5F, and (e-h) the corresponding 2D GISAXS patterns. (i) 1D GIWAXS profiles along the q_z direction, and (j) 1D GISAXS profiles along the q_{xy} axis, with the solid lines as fitted curves using a universal model.

Table 2 Fitting parameters of 1D GISAXS profiles of various PBDB-T-2F:BTP-4F films.

Component	ξ [nm]	η [nm]	D	$2R_g$ [nm]
PBDB-T-2F:BTP-4F	13.0	9.5	3.0	46.5
PBDB-T-2F:BTP-4F (INB-1F)	11.8	10.7	3.0	52.4
PBDB-T-2F:BTP-4F (INB-3F)	11.5	11.3	3.0	55.9
PBDB-T-2F:BTP-4F (INB-5F)	10.5	12.9	3.0	63.2

Grazing-incidence small-angle X-ray scattering (GISAXS) measurements were conducted to gain information on the phase-separated domain size within various PBDB-T-2F:BTP-4F blend films (see Fig. 4(e-h)). The 1D GISAXS profiles of various blend films along the IP direction are presented in Fig. 4(j) and are fitted with a universal model using the software SasView. The solid lines in Fig. 4(j) are fitted curves and the best fitting parameters are listed in Table 2. In the table, ξ , η , D , and $2R_g$ represents the average correlation length of the BTP-4F dispersed PBDB-T-2F phase, the correlation length of acceptors, the fractal dimension of acceptors and the size of the aggregated acceptor domain.⁵¹ As we can see from the results, the average correlation length of the BTP-4F dispersed PBDB-T-2F phase reduces whilst the domain size of acceptors increases when the films were processed using the solid additives. This suggests that these additives facilitate the migration of BTP-4F molecules from the PBDB-T-2F phase (which reduces the correlation length of the donor phase) and then form larger aggregates (which increases the correlation length of the acceptor phase). This observation is consistent with our GIWAXS characterization that the BTP-4F π - π stacking becomes stronger after treatment with the additives. Among all these additives, we find INB-5F to be the most effective at increasing the π - π stacking and correlation length of BTP-4F. Although the increase of the correlation length does not facilitate exciton dissociation (as it will reduce the density of heterojunction interfaces), it does improve charge transport as demonstrated above.

In order to understand the interactions of our additives with the electron acceptor BTP-4F, we have performed molecular dynamic simulations. The geometry configuration of additives INB-1F, INB-3F and INB-5F are simulated and illustrated in Fig. 5(a-c). The dihedral angles between the 1H-indene-1, 3(2H)-dione and benzene units of INB-1F, INB-3F and INB-5F are 3.6°, 50.1°, 48.4° respectively. Increasing the number of fluorine atoms in the benzene ring results in a substantial twists of the two molecular units and destroys the planarity of the molecule. Fig. 5(d-f) show the electrostatic potential (ESP) distribution of these additives. The ESP concentration is relatively neutral in the center of INB-1F. Negative ESP gradually concentrates from the indanone to the fluorobenzene unit in INB-3F and INB-5F due to the strong electronegativity of fluorine atoms, leaving the indanone unit positively charged. We firstly determined the interactions between the electron acceptor BTP-4F and additives. Fig. 5(g-i) show the optimal configuration of the adsorption of one INB-1F, INB-3F, INB-5F molecule onto one BTP-4F, respectively. We observed that the additive molecule prefers to stack on the central “D-A-D” unit rather than the two

terminating “A” units of BTP-4F. The adsorption energy of additive on BTP-4F ($E_{\text{BTP-4F/additive}}$) is summarized in Table S4. When the adsorption energy is smaller, the adsorption capacity will be stronger. We determined that all additives tend to adsorb to BTP-4F molecules, amongst which INB-5F shows the strongest adsorption capacity with the lowest adsorption energy of -38.5 kcal/mol. This is associated with the smallest stacking distance between the indanone unit of the additive and the “D-A-D” unit of BTP-4F (see Table S4). Fig. 5(j-m) shows the molecular aggregation states of four BTP-4F molecules with/without the presence of two additive molecules. As summarized in Table S5, the average distance between two BTP-4F molecules reduces from *ca.* 3.6 Å of the system without the presence of any additive to 3.4 Å when the additives are added. The adsorption energies of three BTP-4F molecules on a BTP-4F surface processed with the presence of two INB-1F, INB-3F or INB-5F molecules are all below -200 kcal/mol. These values are much lower than the absorption energy of -152.1 kcal/mol without any additive, implicating that the presence of these additives promotes the π - π stacking tendency of BTP-4F molecules. Our molecular dynamic simulations therefore support that these additives have attractive interactions with BTP-4F via π - π stacking, and their presence reduces the adsorption energy between BTP-4F molecules to improve structural order. These effects are most pronounced with the additive INB-5F, which has five fluorine atoms on the fluorobenzene unit. All these observations are consistent with our morphology and device performance studies presented in the earlier sections.

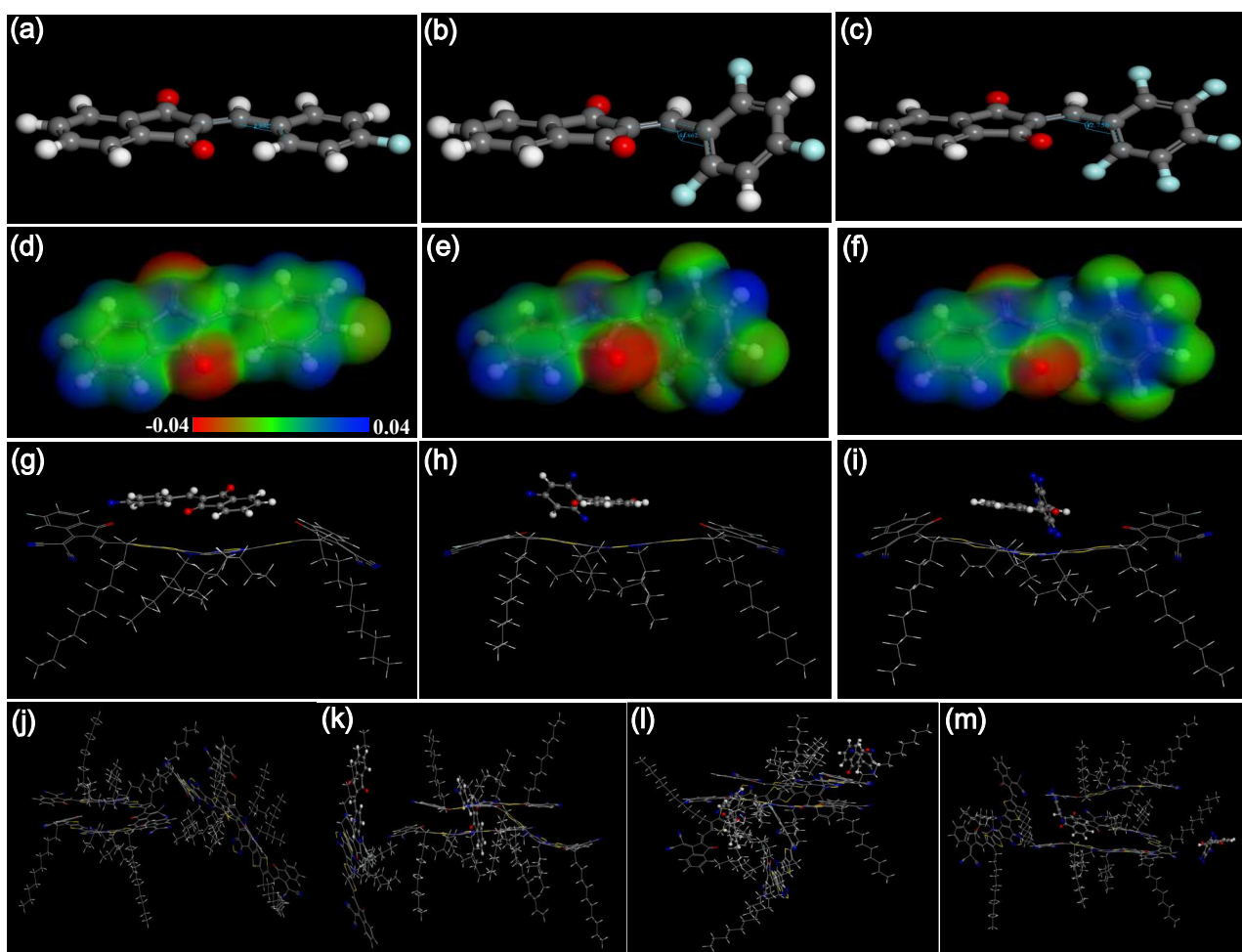


Fig. 5 (a), (b), (c) The optimal geometry configuration and (d), (e), (f) electrostatic potential (ESP) of additive INB-1F, 3F, 5F additives. Optimal configuration of one BTP-4F molecule adsorbing with one (g) INB-1F (h) INB-3F and (i) INB-5F molecule, respectively. Optimal configuration of one BTP-4F molecule adsorbing another three BTP-4F molecules (j) without additives and with the presence of two (k) INB-1F (l) INB-3F, (m) INB-5F molecules.

Finally, the shelf-stability of encapsulated PBDB-T-2F:BTP-4F OSCs devices was investigated. Such devices were tested daily and stored under ambient conditions (at an average temperature of 25°C and humidity around 70%) when they were not being tested. Device metrics are plotted as a function of time for a total period of 30 days in Fig. 6. It can be seen that the V_{OC} of all devices are quite stable and remain largely unchanged after 30 days of storage in air. The J_{SC} and FF of the reference device however drop to below 90% of their initial values, resulting in a PCE of about 80% of the starting value. For the devices processed with additives, the J_{SC} values reduce as storage time increases but at a much lower rate compared to the reference device. Here the INB-5F

processed device exhibits superior shelf stability than either the INB-3F or INB-1F processed devices. The FF degradation rates of these additive processed devices are also improved to a similar level. The PCE degradation rates of these additives processed OSCs are largely a reflection of J_{sc} changes, as the FF and V_{oc} of these devices change at a similar rate. Around 90% of the initial PCE is retained after ambient storage for 30 days, with the INB-5F processed OSCs demonstrating the best stability. We believe that the densely packed photoactive layer processed with these fluorinated additives is the origin of such enhanced stability.

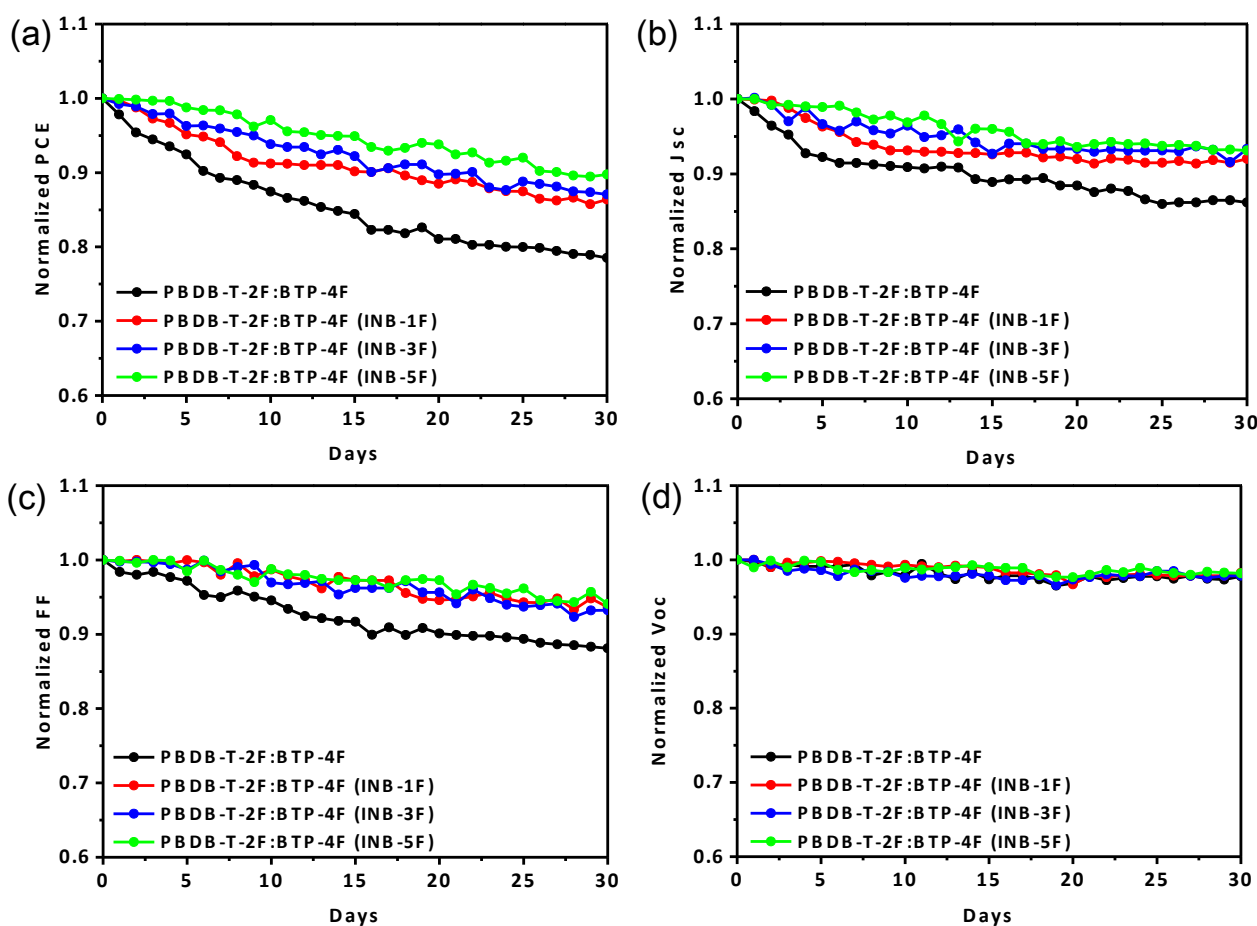


Fig. 6 The evolutions of (a) PCE, (b) J_{sc} , (c) FF, (d) V_{oc} over storage time for encapsulated PBDB-T-2F:BTP-4F OSCs fabricated without or with the presence of different additives.

3. Conclusion

In conclusion, three volatilizable organic solid additives with different degrees of fluorination were designed and synthesized, and have been demonstrated to be effective for regulating the morphology of non-fullerene OSCs, leading to improved device efficiency and stability. These additives evaporate upon thermal annealing and exhibit increased volatility as the number of

fluorine atoms increases. When processed using these additives during solution casting, PBDB-T-2F:BTP-4F non-fullerene OSCs undergo an improvement in efficiency from 15.2% to 16.5%, whilst that of PBDB-T-2F:IT-4F improve from 12.1% to 13.4%. Grazing-incidence X-ray studies show that the fluorinated additives, especially INB-5F, can significantly enhance the π - π stacking among electron acceptors, leading to slightly larger acceptor domain size that improves electron mobility. Molecular dynamic simulations shows that the additives have attractive interactions with BTP-4F via π - π stacking, and that their presence reduces the adsorption energy among BTP-4F molecules to promote structural order. The additive processed devices also exhibit enhanced long-term storage stability. Our work demonstrates a promising strategy to design new solid additives to effectively improve the device performance of non-fullerene organic solar cell.

Supporting Information

The Supporting Information is available from the RSC Online Library or from the author.

Acknowledgements

The work was supported by the National Natural Science Foundation of China (Grants No. 21774097) and the Natural Science Foundation of Hubei Province of China (Grant No. 2018CFA055). All authors thank the beamline BL16B1 at Shanghai Synchrotron Radiation Facility (China) for providing the beam time and for the help of staff during experiments. We also thank the UK EPSRC for studentships for R.C.K. and J.A.S. (via EPSRC Centre for Doctoral Training in New and Sustainable PV EP/L01551X/1). The GIWAXS measurements were performed on the Sheffield Xeuss 2.0 instrument, and we are indebted to Xenocs for their ongoing help and support in the user program at The University of Sheffield.

Conflict of Interest

The authors declare no conflict of interest.

References

- 1 H. Chen, J. Hou, S. Zhang, Y. Liang, G. Yang, Y. Yang, L. Yu, Y. Wu and G. Li, *Nat. Photonics.*, 2009, **3**, 649.
- 2 A. J. Heeger, *Adv. Mater.*, 2014, **26**, 10.
- 3 G. Li, R. Zhu and Y. Yang, *Nat. Photonics.*, 2012, **6**, 153.
- 4 L. Lu, T. Zheng, Q. Wu, A. M. Schneider, D. Zhao and L. Yu, *Chem. Rev.*, 2015, **115**, 12666.

- 5 P. Cheng, G. Li, X. Zhan and Y. Yang, *Nat. Photonics.*, 2018, **12**, 131.
- 6 V. V. Brus, J. Lee, B. Luginbuhl, S. Ko, G. C. Bazan and T. Nguyen, *Adv. Mater.*, 2019, **31**, 1900904
- 7 J. Lee, S. Ko, H. Lee, J. Huang, Z. Zhu, M. Seifrid, J. Vollbrecht, V. V. Brus, A. Karki, H. Wang, K. Cho, T. Nguyen, and G. C. Bazan, *ACS Energy Lett.*, 2019, **4**, 1401
- 8 X. Xu, K. Feng, Z. Bi, W. Ma, G. Zhang and Q. Peng, *Adv. Mater.*, 2019, **31**, 1901872.
- 9 Y. Cui, H. Yao, J. Zhang, T. Zhang, Y. Wang, L. Hong, K. Xian, B. Xu, S. Zhang, J. Peng, Z. Wei, F. Gao and J. Hou, *Nat. Commun.*, 2019, **10**, 2515.
- 10 J. Yuan, Y. Zhang, L. Zhou, G. Zhang, H.-L. Yip, T.-K. Lau, X. Lu, C. Zhu, H. Peng, P. A. Johnson, M. Leclerc, Y. Cao, J. Ulanski, Y. Li and Y. Zou, *Joule.*, 2019, **3**, 1140.
- 11 J. Hou, O. Inganä, R. H. Friend and F. Gao, *Nat. Mater.*, 2018, **30**, 5429.
- 12 Y. Lin, J. Wang, Z. Zhang, H. Bai, Y. Li, D. Zhu and X. Zhan, *Adv. Mater.*, 2015, **27**, 1170.
- 13 H. Fu, Z. Wang and Y. Sun, *Angew. Chem. Int. Ed.*, 2019, **131**, 4488.
- 14 R. S. Gurney, D. G. Lidzey and T. Wang, *Rep. Prog. Phys.*, 2019, **82**, 036601.
- 15 W. Li, M. Chen, J. Cai, E. L. K. Spooner, H. Zhang, R. S. Gurney, D. Liu, Z. Xiao, D. G. Lidzey, L. Ding and T. Wang, *Joule.*, 2019, **3**, 819.
- 16 Y. Yan, W. Li, J. Cai, M. Chen, Y. Mao, X. Chen, R. S. Gurney, D. Liu, F. Huang and T. Wang, *Mater. Chem. Front.*, 2018, **2**, 1859.
- 17 Y. Bai, C. Zhao, X. Chen, S. Zhang, S. Zhang, T. Hayat, A. Alsaedi, Z. Tan, J. Hou and Y. Li, *J. Mater. Chem. A.*, 2019, **7**, 15887.
- 18 J. Huang, H. Wang, K. Yan, X. Zhang, H. Chen, C. Z. Li and J. Yu, *Adv. Mater.*, 2017, **29**, 1606729
- 19 M. Li, K. Gao, X. Wan, Q. Zhang, B. Kan, R. Xia, F. Liu, X. Yang, H. Feng, W. Ni, Y. Wang, J. Peng, H. Zhang, Z. Liang, H. L. Yip, X. Peng, Y. Cao and Y. Chen, *Nat. Photonics.*, 2017, **11**, 85.
- 20 B. Fan, D. Zhang, M. Li, W. Zhong, Z. Zeng, L. Ying, F. Huang and Y. Cao, *Sci. China Chem.*, 2019, **62**, 746.
- 21 L. Meng, Y. Zhang, X. Wan, C. Li, X. Zhang, Y. Wang, X. Ke, Z. Xiao, L. Ding, R. Xia, H. L. Yip, Y. Cao and Y. Chen, *Science.*, 2018, **361**, 1094.
- 22 H. Sun, T. Liu, J. Yu, T. Lau, G. Zhang, Y. Zhang, M. Su, Y. Tang, R. Ma, B. Liu, J. Liang, K. Feng, X. Lu, X. Guo, F. Gao and H. Yan, *Energy Environ. Sci.*, 2019, **12**, 3328.

- 23 T. Yan, W. Song, J. Huang, R. Peng, L. Huang and Z. Ge, *Adv. Mater.*, 2019, **31**, 1902210.
- 24 Q. An, X. Ma, J. Gao and F. Zhang, *Sci. Bull.*, 2019, **64**, 504.
- 25 X. Ma, Q. An, O. A. Ibraikulov, P. L'evêque, T. Heiser, N. Leclerc, X. Zhang and F. Zhang, *J. Mater. Chem. A.*, 2020, **8**, 1265.
- 26 X. Ma, J. Wang, Q. An, J. Gao, Z. Hu, C. Xu, X. Zhang, Z. Liu and F. Zhang, *Nano Energy.*, 2020, **70**, 104496.
- 27 J. Gao, J. Wang, Q. An, X. Ma, Z. Hu, C. Xu, X. Zhang and F. Zhang, *Sci China Chem.*, 2020, **63**, 83.
- 28 J. Gao, W. Gao, X. Ma, Z. Hu, C. Xu, X. Wang, Q. An, C. Yang, X. Zhang and F. Zhang, *Energy Environ Sci.*, 2020, DOI: 10.1039/C9EE04020J.
- 29 T. Zhang, H. Han, Y. Zou, Y.-C. Lee, H. Oshima, K.-T. Wong and R. J. Holmes, *ACS Appl. Mater. Interfaces.*, 2017, **9**, 25418.
- 30 W. Ma, C. Yang, X. Gong, K. Lee and A. J. Heeger, *Adv. Funct. Mater.*, 2005, **15**, 1617.
- 31 M. Li, F. Liu, X. Wan, W. Ni, B. Kan, H. Feng, Q. Zhang, X. Yang, Y. Wang, Y. Zhang, Y. Shen, T. P. Russell and Y. Chen, *Adv. Mater.*, 2015, **27**, 6296.
- 32 G. Li, Y. Yao, H. Yang, V. Shrotriya, G. Yang and Y. Yang, *Adv. Funct. Mater.*, 2007, **17**, 1636.
- 33 W. Li, M. Chen, Z. Zhang, J. Cai, H. Zhang, R. S. Gurney, D. Liu, J. Yu, W. Tang and T. Wang, *Adv. Funct. Mater.*, 2018, **29**, 1807662.
- 34 H. Liao, C. Ho, C. Chang, M. Jao, S. B. Darling and W. Su, *Mater. Today.*, 2013, **16**, 326.
- 35 L. Tan, P. Li, Q. Zhang, R. Izquierdo, M. Chaker and D. Ma, *ACS Appl. Mater. Interfaces.*, 2018, **10**, 6498.
- 36 K. L. Jae, L. M. Wan, C. J. Brabec, J. Yuen, S. M. Ji, Y. K. Jin, K. Lee, G. C. Bazan and A. J. Heeger, *J. Am. Chem. Soc.*, 2008, **130**, 3619.
- 37 M. T. Dang and J. D. Wuest, *Chem. Soc. Rev.*, 2013, **42**, 9105.
- 38 C. McDowell, M. Abdelsamie, M. F. Toney and G. C. Bazan, *Adv. Mater.*, 2018, **30**, 1707114.
- 39 G. Ren, E. Ahmed and S. A. Jenekhe, *Adv. Energy Mater.*, 2011, **1**, 946.
- 40 H. Choi, S.-J. Ko, T. Kim, P.-O. Morin, B. Walker, B. H. Lee, M. Leclerc, J. Y. Kim and A. J. Heeger, *Adv. Mater.*, 2015, **27**, 3318.
- 41 C. V. Hoven, X. Dang, R. C. Coffin, J. Peet, T. Nguyen and G. C. Bazan, *Adv. Mater.*, 2010,

22, E63.

- 42 B. J. Tremolet de Villers, K. A. O'Hara, D. P. Ostrowski, P. H. Biddle, S. E. Shaheen, M. L. Chabiny, D. C. Olson and N. Kopidakis, *Chem. Mater.*, 2016, **28**, 876.
- 43 A. Tournebize, A. Rivaton, H. Peisert and T. Chassé, *J. Phys. Chem. C.*, 2015, **119**, 9142.
- 44 X. Song, N. Gasparini and D. Baran, *Adv. Electron. Mater.*, 2018, **4**, 1700358.
- 45 R. Yu, H. Yao, L. Hong, Y. Qin, J. Zhu, Y. Cui, S. Li and J. Hou, *Nat. Commun.*, 2018, **9**, 4645.
- 46 R. Yu, H. Yao, Z. Chen, J. Xin, L. Hong, Y. Xu, Y. Zu, W. Ma and J. Hou, *Adv. Mater.*, 2019, **31**, 1900477.
- 47 R. Sun, J. Guo, Q. Wu, Z. Zhang, W. Yang, X. Jiao, H. Ade, W. Tang, C. J. Brabec and J. Min, *Energy Environ. Sci.*, 2019, **12**, 3118.
- 48 G. G. Malliaras, J. R. Salem, P. J. Brock and C. Scott, *Phys. Rev. B.*, 1998, **58**, R13411.
- 49 J. Vollbrecht, V. V. Brus, S. Ko, J. Lee, A. Karki, D. Cao, K. Cho, G. C. Bazan, and T. Nguyen, *Adv Energy Mater.*, 2019, **9**, 1901438.
- 50 S. Hosseini, S. Roland, J. Kurpiers, Z. Chen, K. Zhang, F. Huang, A. Armin and D. Neher, *J. Phys. Chem. C.*, 2019, **123**, 6823.
- 51 W. Li, J. Cai, Y. Yan, F. Cai, S. Li, R. S. Gurney, D. Liu, J. D. McGettrick, T. M. Watson, Z. Li, A. J. Pearson, D. G. Lidzey, J. Hou and T. Wang, *Sol. RRL.*, 2018, **2**, 1800114.